# Compact Digital Microrobot Based on Multistable Modules

A. Mohand-Ousaid[1], I. Bouhadda[1], G. Bourbon[1], P. Le Moal[1], Y. Haddab[2] and P. Lutz[1]

***Abstract*— Current digital microrobots are mainly composed of bistable modules and flexible structures. Unlike conventional microrobots, they are based on mechanical stability instead of complex control strategies in order to reach precise and repeatable discrete positioning. By design, their number of stable positions depends on the number of bistable modules. As a consequence, increasing the robot workspace requires using several modules. In this case, the robot size increases and its miniaturization becomes complex and non-intuitive. To address this issue, a multistable module has been developed to reach several stable positions. In this paper, a new generation of digital microrobots is proposed. Based on two multistable modules and flexible structures, the new microrobot can reach a large workspace while having a small footprint. Concretely, the robot size decreases by 26% while the number of stable positions increases by 950% in comparison with the first generation of the digital microrobot. A prototype is designed, fabricated and characterized experimentally. Preliminary results show a good agreement between the expected and the achieved workspace. The robot achieves 169 stable positions with a discrete step of 4.125 $\mu$m and a resolution of 150 nm. With these capabilities, the robot paves the way for promising perspectives and applications, in particular precise micro-manipulation in confined environment such as a Scanning Electron Microscope.**

## I. INTRODUCTION

The development of miniaturized products we use every day is growing increasingly during the two last decades. In this regard, there is a clear need for accurate micro-manipulation tools. For instance, watch micromechanisms, medical and bio-medical devices, microsystems, optic and electronic devices are products that require efficient and reliable micromanipulation tools for their assembly [1]. Thanks to the progress in the field of smart materials several micro-robotic systems are developed for this purpose. Considering their output displacements, they can be classified into two main categories: microrobots with proportional (continuous) displacements and microrobots with incremental (discrete) displacements.

The first category uses proportional actuation to generate continuous displacements [1], [2]. Unlike conventional actuators, smart materials such as piezoelectric materials are particularly privileged for their design since they are suitable and compatible for miniaturization. However, despite their intrinsic high resolution and high dynamics, these materials have some drawbacks. They often exhibit nonlinear and non-stationary behavior. They are also sensitive to environmental conditions such as temperature and humidity [3]. Under these conditions, their design becomes a complex task that requires tiny sensors and bulky instruments for signal processing.

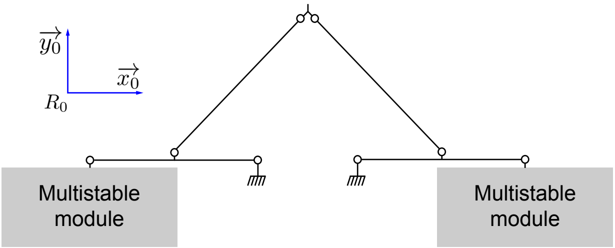

Fig. 1. Sketch architecture of the second generation of digital microrobot.

In contrast, the second category namely digital micro-robotics uses discrete actuation to generate incremental displacement without closed-loop control (no need for sensors). Inspired by binary paradigm of robotic manipulators [4], these robots are based on bistable mechanisms [5]–[11] that generate a displacement between two stable positions (0 and 1). As a consequence, the digital robots guarantee mechanical stability, high accuracy, and the repeatability of their discrete workspace positions in open-loop without energy consumption unlike stick-slip [12], inertial [13] or inchworms actuators [14], [16]. As reported in [17], this concept is successfully employed to design a digital microrobot suitable for micromanipulation in confined environments such as Scanning Electron Microscope (SEM). Named DiMiBot, it is referred to as the first generation of digital microrobot. It is basically composed of four bistable modules and their elementary displacements are transmitted to the tip of the robot through flexible structures. With this configuration, the robot is able to reach 16 stable positions. Although this microrobot shows great potential, it is subjected to a trade-off between the stable positions and the dimensions of the mechanism. When several bistables are combined, the size of the robot increases rapidly. Thus, the miniaturization and the calculation of the robot forward and inverse kinematics become complex and non-intuitive.

To overcome this limitation, a multistable module has been investigated in [18]. Compared to a bistable module, it allows switching its moving part between 13 stable positions. Leveraging multistable modules, this paper investigates the second generation of digital microrobots. As illustrated in Fig. 1, the robot comprises two multistable modules and flexible structures. The main advantages of this new microrobot structure are summarized as follows:

- The microrobot can reach a large workspace while having a smaller footprint. In comparison with the previous generation (544 mm$^2$/16 stable positions), the new generation has a footprint of 400 mm$^2$ and can generate 169 stable positions. In other words, the size

---

[1] are with Université Bourgogne Franche-Comté, FEMTO-ST Institute/CNRS, Besançon, France.
[2] is with Université de Montpellier, LIRMM/CNRS, Montpellier, France.

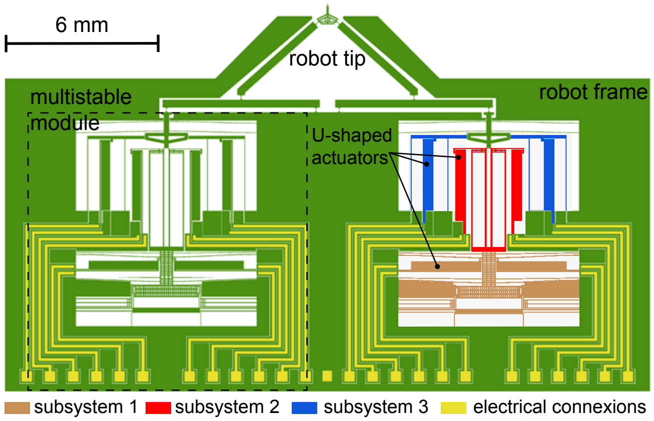

Fig. 2. CAD model of the digital microrobot.

of the robot decreases by 26% while the number of stable position increases by 950%.

- The microrobot architecture being simplified makes easy the calculation of the forward and the inverse kinematics models.
- The microrobot fabrication and control become simpler since only two multistable modules are used.

A mechanical structure of the robot is proposed and its forward and inverse kinematics are calculated. Then, a prototype is fabricated on SOI wafer using a deep reactive ion etching based process (DRIE). Simulations are carried out to validate the forward kinematics model, while experiments are conducted to characterize the robot functional principle and its workspace. Preliminary results show a good agreement between the simulated and the achieved workspace. As expected, the microrobot generates 169 stable positions with a discrete step of 4.125 $\mu$m and a resolution of 150 nm. Having these capabilities, this new generation opens a promising perspective for precise micromanipulation applications in confined environments where the working space is becoming smaller and smaller.

## II. Second generation of digital micorobots

This section focuses on the mechanical design of the second generation of digital microrobots. It describes mainly the proposed architecture, its advantages, and its principle of functioning.

### A. Microrobot architecture

The CAD model given in Fig 2 shows how the architecture given in Fig. 1 is implemented. The model reports all the details including the actuators and their connections with the robot tip. Likewise the previous generation, a symmetrical architecture is used, however, it comprises only two multistable modules. Each module is connected to the robot tip through flexible structures that convert their elementary unidirectional displacements to to bidirectional displacements. This new architecture, compact and easy to implement, can reach a larger workspace by combining several stable positions.

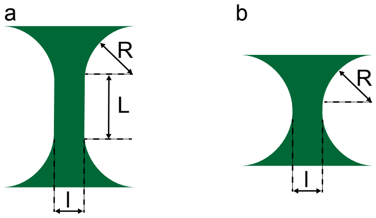

Fig. 3. Flexible hinges. a) corner-filleted flexible hinge, b) circular flexible hinge.

### B. Multistable module

As can be seen in Fig. 2, the multistable module is the cornerstone of the digital robot architecture. Only two modules are sufficient to generate a large workspace while having a small footprint. The whole module comprises three subsystems that guarantee the switching, the holding, and the guiding of its moving part. Each subsystem consists of flexible structures actuated by two U-shaped actuators. Each actuator can provide respectively a displacement of 200 $\mu$m and a force higher than 10 mN, which are largely sufficient to actuate the multistatble and the whole robot. When the actuators are activated in a specific sequence, their combination allows generating 13 stable positions (from 0 to 12) with a step of 10 mm. Reader can refer to [15] for more detail about the design, the fabrication, and the characterization of multistable modules. He/She can also refer to [16] for the repeatability and the reproducibility characterization of multistable modules.

### C. Flexible structures

Figures 1 and 2 show how the robot tip and flexible structures are connected. The connection consists of a serial kinematic chain that transmits the module displacements to the robot tip. In this chain, a horizontal link (x-axis) is connected to the multistable moving part through a flexible hinge at one side while the other side is connected to a clamped hinge. Following, a diagonal link connects the middle of the horizontal link and the robot tip through hinges. Such combination results in a parallel kinematic chain that converts the vertical displacements of modules to planar displacements at the robot tip.

### D. Flexible hinges dimensioning

Flexible hinges are commonly used to design micro-nanosystems with high resolution. Thanks to their monolithic structure, they do not involve mechanical backlash and friction between parts that usually affect the accuracy of the system. Here, corner-filleted flexible hinge illustrated in Fig. 3.a (represented by a circle in Fig 1) with the same dimensions are particularly used for two reasons: (i) it mimics the behavior of a traditional revolute joint and (ii) provides a large deformation in comparison with simple circular hinge (see Fig. 3.b). Unlike rectangular or ellipse hinges [20], they generate an accurate rotation with an approximately fixed center of rotation. However, due to their size, they give rise to two main constraints: (i) when subjected to deformation they produce high stress that may cause irreversible deformation

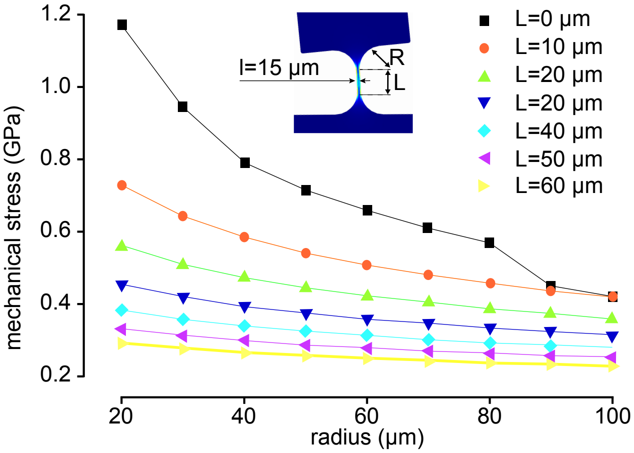

Fig. 4. Mechanical stress versus hinge radius and straight beam segment length.

or breakage (ii) their fabrication in particular over-etching could make the robot structure fragile. To prevent these constraints, the optimal dimensions of the hinges have to be determined. As illustrated in Fig. 3.a, three main dimensions are concerned: $L$ the length of the straight beam segment, $R$ the radius of the hinge, and $l$ the minimum engraving width. First of all, by considering the fabrication process limitation, the parameter $l$ is chosen to be 15 $\mu m$. This allows minimizing the effect of over-etching that may weaken the robot structure knowing that this phenomenon induces about 2 $\mu m$ uncertainty. Then, FEA simulations under COMSOL are carried out to find the parameters $L$ and $R$. Figure 4 reports the mechanical stress curves versus the hinge radius $R$ for different values of $L$ while $l$ is kept fix and equals to 15 $\mu m$. For each configuration, the mechanical stress is evaluated for deformation of 120 $\mu m$ which is the maximum displacement that can be generated by a multistable module. According to the simulations and the stress limit of the silicon material considered here as ∼0.5 GPa, we selected $R = 60$ $\mu m$ and $L = 60$ $\mu m$ in order to guarantee a good behavior of the flexible hinges. It is worth to notice that $R$ and $L$ can be increased to decrease the mechanical stress, however, the hinge will become less precise in keeping the position of the rotation center as reported in [21].

### E. Principle of functioning

To reach any position within the workspace, the robot combines vertical displacements of modules and deformations of flexible structures. The displacement sequence starts by converting the targeted position into a binary sequence. This sequence corresponds to the number of elementary steps that both modules have to generate. Each elementary step revolves around several sub-steps that include: moving, opening, and closing of the multistable clamps with or without its moving part. a similar sequence is, then, repeated to generate several successive upward or downward steps. For further details about the combination and the control sequence order that allows generating a displacement step, reader can refer to [18]. Throughout the process, the horizontal rigid links are subjected to the same displacements as moving parts of modules. In return, the horizontal link drives the diagonal link which transmits the deformation to the robot tip.

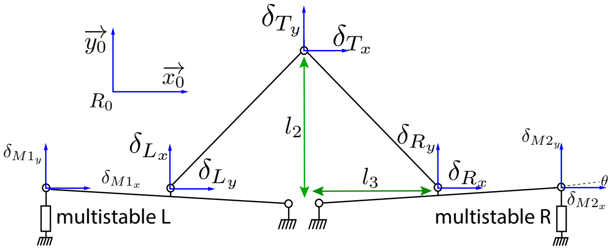

Fig. 5. Simplified microrobot kinematics.

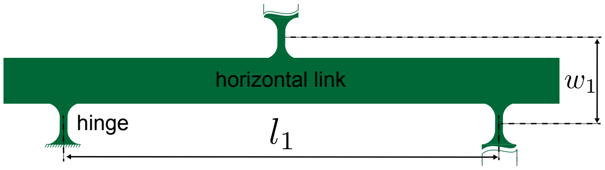

Fig. 6. Horizontal and vertical distances between hinges.

## III. MICROROBOT'S KINEMATICS

This section deals with the calculation of the robot forward and inverse kinematics models. Unlike the previous generation, the calculation is simpler since the robot has a simple architecture, actuated with only two multistable modules. Furthermore, the following assumptions are considered for practical reasons:

1- Links are rigid (deformations are located within the hinges).
2- Rotations take place at the center of the hinges (perfect joints).
3- Induced rotations are considered small.

All these assumptions are due to the robot displacements, which are very small in comparison with the robot structure.

### A. Forward kinematics

The forward kinematics model expresses the displacement of the robot tip ($\delta_{T_x}$, $\delta_{T_y}$) as a function of multistable states ($M_1$ and $M_2$, which can vary from 0 to 12) and the geometrical parameters of the robot. Based on the kinematics scheme given in Fig. 5, the model is calculated in several steps. We started by expressing the tip displacements according to the displacements of points $L$ and $R$, noted $\delta_{L_x}$, $\delta_{L_y}$ and $\delta_{R_x}$, $\delta_{R_y}$, respectively. By taking in consideration the geometrical parameters $l_2$ and $l_3$ (see Fig. 5), this relationship can be expressed as (1):

$$\begin{Bmatrix} \delta_{T_x} \\ \delta_{T_y} \end{Bmatrix} = \frac{1}{2} \begin{bmatrix} 1 & \frac{l_2}{l_3} & 1 & -\frac{l_2}{l_3} \\ \frac{l_3}{l_2} & 1 & -\frac{l_3}{l_2} & 1 \end{bmatrix} \begin{Bmatrix} \delta_{L_x} \\ \delta_{L_y} \\ \delta_{R_x} \\ \delta_{R_y} \end{Bmatrix} \qquad (1)$$

Then, we expressed the displacements of points $L$ and $R$ according to the multistable states. Taking into account the horizontal and the vertical distances between two hinges, $l_1$

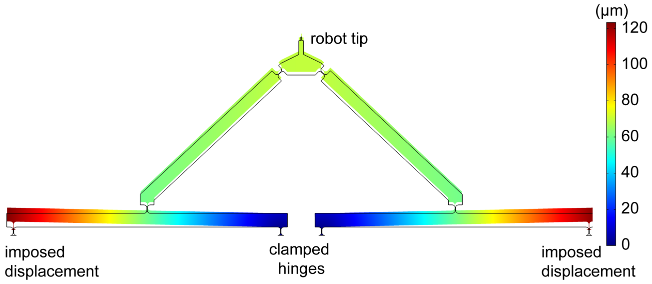

Fig. 7. FEA simulation of the robot workspace. Case where each module generates a displacement of 120 $\mu$m ($M_1$=$M_2$=12).

and $w_1$ respectively, which are the same for the left link (see Fig.6), the relationship can be expressed as:

$$\begin{Bmatrix} \delta_{L_x} \\ \delta_{L_y} \end{Bmatrix} = \begin{bmatrix} \frac{l_1}{2}(cos(\theta)-1)+w_1 sin(\theta) \\ \frac{l_1}{2} sin(\theta)+w_1(cos(\theta)-1) \end{bmatrix} \tag{2}$$

Considering small angles approximation, $\theta = \frac{\delta_{M1_y}}{l_1}$ and displacements of the first module ($\delta_{M1_x}=0$ and $\delta_{M1_y}=\triangle \times M_1$, where $\triangle$ is the module step and $M_1$ is the state of the first multistable.) the relationship 2 can be written as:

$$\begin{Bmatrix} \delta_{L_x} \\ \delta_{L_y} \end{Bmatrix} = \begin{bmatrix} \frac{w_1}{l_1} \times \triangle \\ \frac{1}{2} \times \triangle \end{bmatrix} M_1 \tag{3}$$

The same reasoning is applied to multistable 2 and leads to the following relationship between displacements of point R and displacements of module 2.

$$\begin{Bmatrix} \delta_{R_x} \\ \delta_{R_y} \end{Bmatrix} = \begin{bmatrix} -\frac{w_1}{l_1} \times \triangle \\ \frac{1}{2} \times \triangle \end{bmatrix} M_2 \tag{4}$$

Finally, we substituted equations (3) and (4) in equation (1), which leads to the robot forward kinematics model:

$$\begin{Bmatrix} \delta_{T_x} \\ \delta_{T_y} \end{Bmatrix} = \frac{\triangle}{2} \begin{bmatrix} \frac{w_1}{l_1}+\frac{l_2}{2l_3} & -\frac{w_1}{l_1}-\frac{l_2}{2l_3} \\ \frac{l_3 w_1}{l_2 l_1}+\frac{1}{2} & \frac{l_3 w_1}{l_2 l_1}+\frac{1}{2} \end{bmatrix} \begin{Bmatrix} M_1 \\ M_2 \end{Bmatrix} \tag{5}$$

By considering $K=\frac{\triangle}{2}(\frac{w_1}{l_1}+\frac{l_2}{2l_3})$ as a common factor, the forward kinematics model can be rewritten as:

$$\begin{Bmatrix} \delta_{T_x} \\ \delta_{T_y} \end{Bmatrix} = K \begin{bmatrix} 1 & -1 \\ \frac{l_3}{l_2} & \frac{l_3}{l_2} \end{bmatrix} \begin{Bmatrix} M_1 \\ M_2 \end{Bmatrix} \tag{6}$$

This model permits to derive the theoretical robot discrete step and the robot workspace size. The first one concerns the distance between two neighboring positions. It corresponds to the tip displacements that result when one module generates a step. By substituting $[M_1 \quad M_2]^T$ by $[1 \quad 0]^T$, the discrete step of the workspace equals $r=\frac{\triangle}{2}(\frac{w_1}{l_1}+\frac{l_2}{2l_3})\sqrt{(1+(\frac{l_3}{l_2})^2)}$. The second one concerns the maximum reachable robot workspace. As the robot uses two similar modules, it has the same size along $\overrightarrow{x}$ and $\overrightarrow{y}$ axes and corresponds to $(M-1)r$, where $M$ is the number of module states.

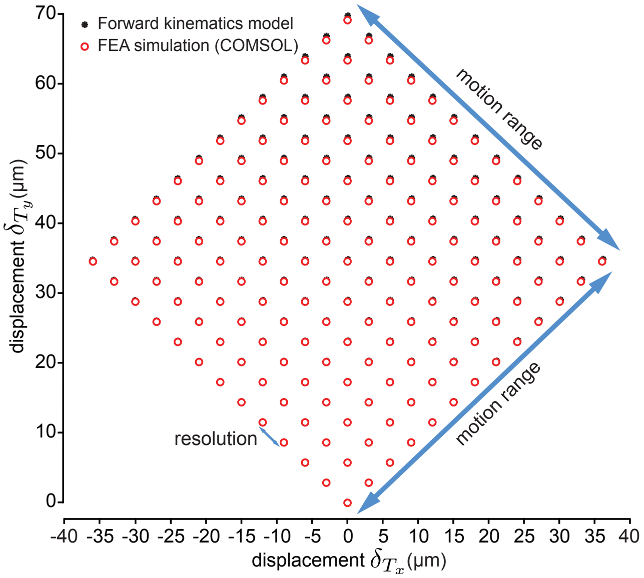

Fig. 8. Theoretical versus simulated microrobot workspace.

TABLE I

COMPARISON BETWEEN MODEL CALCULATION (MATLAB) AND FEA SIMULATION (COMSOL).

| | generated step | motion range |
|---|---|---|
| MATLAB (FKM) | 4.289 ($\mu$m) | 51.473 ($\mu$m) |
| COMSOL (FEA) | 4.318 ($\mu$m) | 51.816 ($\mu$m) |
| Error | 0.6% | 0.66% |

### *B. Microrobot workspace*

Likewise DiMiBot, the robot generates a 2D discrete workspace. However, the number of achieved positions increases with the use of multistable modules. By considering the multistable discrete step ($\triangle$=10 $\mu m$), the vertical as well as the horizontal distance between two hinges, $w_1 = 480$ $\mu m$ and $l_1 = 5.9$ mm, and the geometrical parameters $l_2 = 3.2$ mm and $l_3 = 2.89$ mm, we evaluated the theoretical workspace by using the forward kinematics model given in equation 6. Then, we carried out FEA analysis under COMSOL multi-physics software for numerical evaluation of the workspace. For simplicity, we considered only the flexible structures shown in Fig. 7. Two of the hinges located on the horizontal link are clamped (blue part) while discrete displacements from 0 to 120$\mu$m with a step of 10 $\mu$m are imposed on the other hinges (red part) to simulate the behavior of the multistable modules. Both results are reported in Fig. 8. As can be seen, the robot can generate 13x13=169 discrete positions arranged inside a square-shaped workspace. On the other hand, Tab. I reports the difference between the FEA analysis and the forward kinematics model. Two metrics are considered: (i) the generated step and (ii) the motion range, i.e, the maximum diagonal straight line that the robot can reach when one multistable is activated from step 0 to step 12 while the other multistable is maintained to a given position. With an error of 0.6% and 0.66%, differences are negligible compared to the resolution of the workspace, thus validating the forward kinematics model.

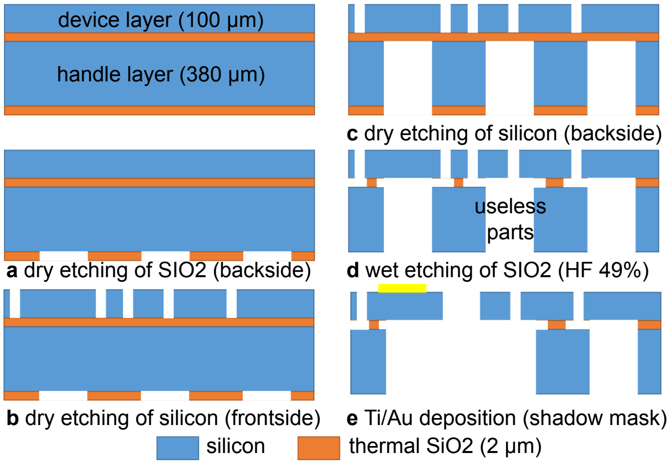

Fig. 9. Clean room fabrication process.

### C. *Inverse kinematics*

The inverse kinematics model expresses the state of modules according to the robot tip position within the workspace. Unlike DiMiBot or classical digital robots, the robot proposed here has a linear forward kinematics model. Therefore, a simple inversion of the forward kinematics model followed by a round function leads to the inverse kinematics model. In this case, the inverse model can be expressed as:

$$\begin{Bmatrix} M_1 \\ M_2 \end{Bmatrix} = round(K^{-1} \begin{bmatrix} 1 & -1 \\ \frac{l_3}{l_2} & \frac{l_3}{l_2} \end{bmatrix}^{-1} \begin{Bmatrix} \delta_{T_x} \\ \delta_{T_y} \end{Bmatrix}) \qquad (7)$$

## IV. MICROFABRICATION

The microrobot is fabricated as a monolithic structure using a single-crystalline silicon-on-insulator (SOI) wafer. As illustrated in Fig. 9, the wafer is composed of four distinct layers: (i) a 100 $\mu$m thick silicon layer dedicated to the active area, (ii) a 2 $\mu$m thick silicon dioxide insulation layer, (iii) a 380 $\mu$m thick handle silicon layer and (iv) a 2 $\mu$m thick silicon dioxide layer serves as a hard mask. As the robot uses two modules, its cleanroom fabrication process follows the same process developed for multistable modules. As reported in [18], the fabrication process revolves around five sub-steps:

1- Patterning and dry etching of the wafer backside using reactive ion etching (RIE) process with an opening window of 60 $\mu m$ (see Fig. 9.a).
2- Patterning and dry etching of the wafer front side with an opening window of 20 $\mu m$ (see Fig.9.b).
3- Dry etching of the handle layer (backside layer) using the DRIE process (see Fig.9.c).
4- Release useless parts by diving the wafer into a hydrofluoric acid (HF 49%) and transversely etching the buried silicon dioxide located between the device and handle openings using HF solution. (see Fig.9.d).
5- Deposition of gold layer of 200 nm thick through a shadow mask (see Fig.9.e).

Achieving all these sub-steps leads to the prototype shown in Fig. 10. After activating the two multistable modules (see [18] for more details about the activation procedure), the device is glued on a PCB card, and a wire bonding is performed for electrical connection.

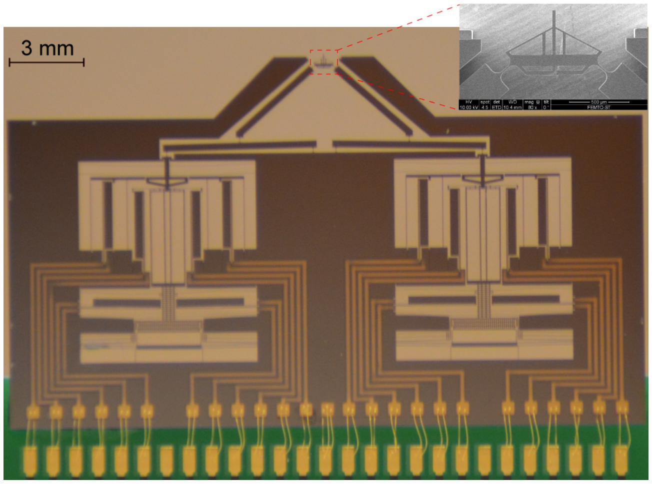

Fig. 10. Fabricated prototype.

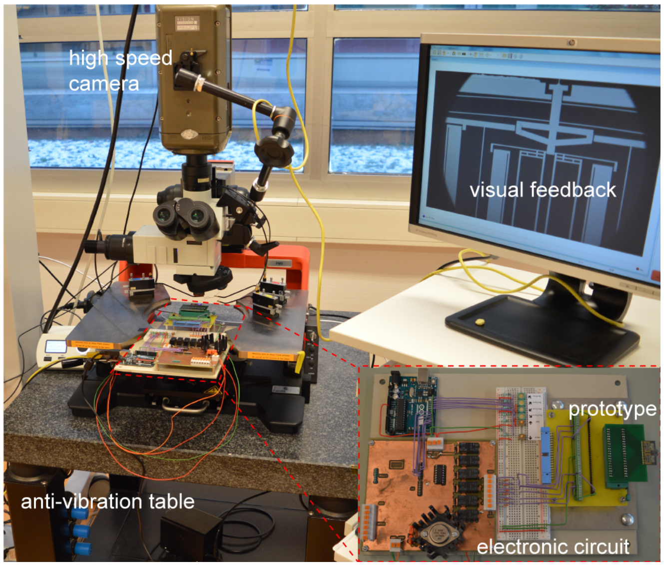

Fig. 11. Experimental Bench.

## V. EXPERIMENTAL CHARACTERIZATION

This section aims to characterize the fabricated robot. It considers two main aspects: (i) the robot working principle and (ii) the robot workspace.

### A. *Experimental bench*

Figure 11 depicts the experimental bench implemented for this study. It comprises a high-speed camera, an electronic circuit, and the microrobot prototype. During the characterization, the microrobot is placed on an anti-vibration table to guarantee the most favorable experimental conditions. It is also dissociated from the electronic circuit to avoid any vibrations that may be induced by relay switching movements. On the other hand, the PCB is connected to the electronic circuit to supply the robot actuators. Based on an Arduino controller, connectors, and relays, this circuit

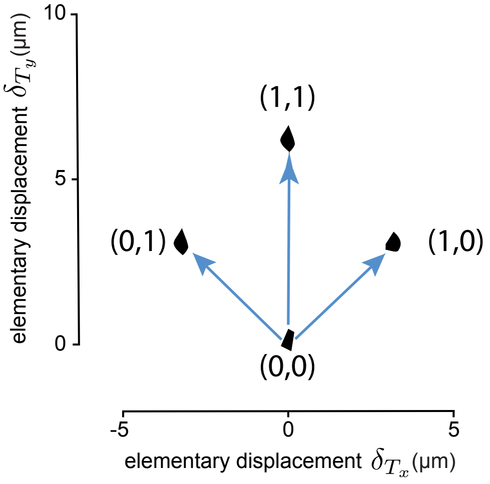

Fig. 12. Elementary displacements of the microrobot tip.

controls the supply time of the control sequences of the U-shaped actuators. Each relay allows switching on/off the current of an electrothermal actuator stage. Otherwise, the circuit uses buttons to switch control between upward and downward steps. In return, the robot tip moves from a discrete position to another. By repeating the sequence, the robot tip can scan the whole workspace. These displacements are captured, recorded, processed, and visualized through a high-speed camera.

### B. Tests, results and discussion

*1) Functioning principle:* The robot functional principle is dependent upon the multistable states. Its validation requires three experimental verifications. They consist to validate the elementary displacement of the robot as follows: (i) the left module is active, (ii) the right module is active, and (iii) both modules are active. When the left multistable module generates a step, the tip has to move to the right side of the workspace. In contrast, the tip has to move to the left side of the workspace when the right module generates a step. However, the robot tip has to move vertically when both modules generate a step. Figure 12 reports the displacement of the robot with respect to the above-mentioned cases. As expected, the robot tip reaches three different positions. In this figure, the row vector (L, R), which contains the state of the left (L) and the state of the right (R) multistable represents the elementary positions. The origin here corresponds to the couple (0,0) where the state of multistables is equal to 0. When the left module generates a step, the tip moves to the position (1,0) located on the right side of the workspace. In contrast, the robot tip moves to the position (0,1) located on the left side of the workspace when the right module generates a step. The robot tip can also reach the position (1,1) by combining two successive elementary displacements (left module step followed by the right module step or right module step followed by the left module step). It is clear from this analysis that the result shows a good agreement with the expected functioning principle. Based on these elementary displacements, the robot tip can travel through the whole workspace. This will be the scope of the next experiment, which aims to characterize the robot workspace.

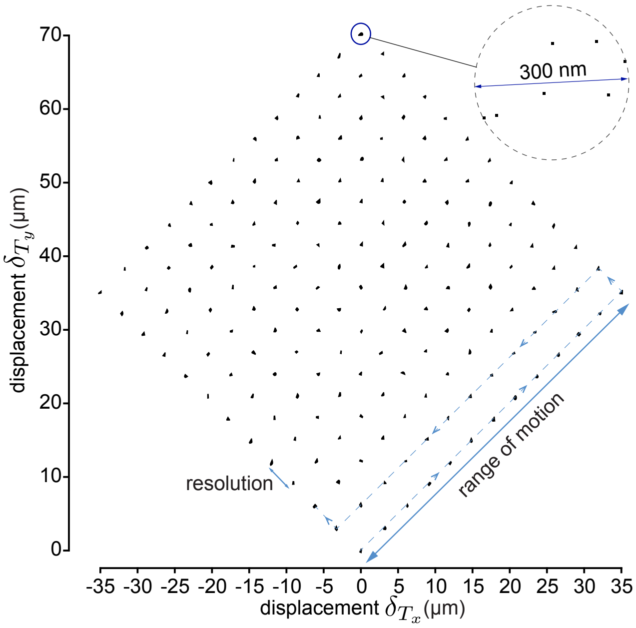

Fig. 13. Experimental characterization of the microrobot workspace.

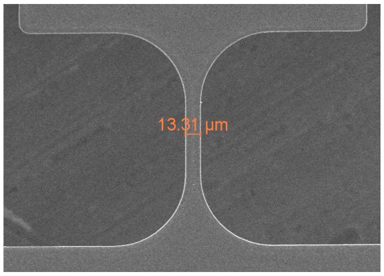

Fig. 14. Effect of over-etching on the geometrical parameters of the hinges.

*2) Workspace:* After demonstrating the functional principle, we characterized the robot workspace and its features using a series of control sequences. First, a series is applied to make the robot tip traveling through the whole space. Starting from the origin, the robot moves to the next positions located in the same diagonal by activating only the left module, which generates 12 upward steps. Then, the only right module generates one upward step to reach the next diagonal. The left module generates again and 12 downward steps to travel along this diagonal. Before repeating the whole cycle, the right module generates again an upward step. The path described by this cycle is illustrated in Fig. 13 (see dashed blue path). Figue 13 reports also the reachable workspace. Each position of this workspace corresponds to a given combination of the robot module states. According to the result, it is trivial that there is a satisfying agreement between the experimental and the simulation data. The robot succeeds to cover 169 discrete positions with a step of 4.125 $\mu$m. Second, the same series is applied seven times to characterize the repeatability of the robot. The set of rules given in [22] are respected to ensure the most favorable

TABLE II

COMPARISON BETWEEN FEA SIMULATION AND EXPERIMENTATION

| | generated step | resolution | motion range |
|---|---|---|---|
| COMSOL (FEA) | 4.318 ($\mu$m) | - | 51.816 ($\mu$m) |
| Experimentation | 4.125 ($\mu$m) | 150 nm | 49,5 ($\mu$m) |
| Error | 4.7% | - | 4.7% |

conditions: same operator, same measurement system (high-speed camera), same operating conditions, same location, and same device for all measurements. For each series, the tip is tracked by a high-speed camera. The resulted data are recorded and then processed to extract the tip displacements. All the obtained displacements are reported in Fig.13. As shown in the zoom (see Fig. 13), the measurements are scattered over a circle with a diameter of 300 nm. This means that the proposed robot can reach a discrete position with a resolution of 150 nm.

Table. II reports the difference between the experimental characterization and the numerical simulation. The difference is calculated for both the generated step and the robot motion range. Unlike the previous comparison, a slight difference (about 4.7%) can be observed between the experiment and the numerical simulation. This difference is mainly due to the over-etching phenomenon that affects the robot structure and its geometrical parameters. For instance, Fig. 14 illustrates the effect of this phenomenon in particular when it comes to fabricate the robot hinges (instead of having a hinge with a width of 15 $\mu$m, we obtained a hinge with a width of 13.31 $\mu$m). Overcoming this phenomenon is challenging, but it would improve the robot resolution and accuracy.

## VI. DISCUSSION

It is clear from the result that the multistable modules open promising perspectives to the design of a new generation of microrobots. It is of particular importance as the number of stable positions and the step resolution can be changed. Indeed, the number of stable positions with the same step can be increased by adding teeth to the multistable moving part and redesigning the guiding beams. On the other hand, the multistable step can vary by modifying the distance between two successive teeth. As can be seen in Fig. 15, the relative distance between two successive teeth fixes the step resolution of the multistable. In our case, this distance is about 10 $\mu$m, which corresponds to the multistable step resolution. Changing this relative distance allows varying the multistable step. From theoretical point of view, a large range of steps can be reached however, the fabrication process limits the minimum step that can be reached because of the etching phenomenon.

## VII. CONCLUSION

This paper presents the design of a new digital microrobot. Unlike the previous generation, it uses two multistable modules and flexible structures. The new microrobot can generate several stable positions while having a small footprint. Starting from the robot sketch the forward kinematics model of the robot is derived under small rotation approximation. Then, the robot workspace features are analyzed theoretically and validated through FEA analysis. The result leads to a workspace composed of 169 positions with a numerical step of 4.318 $\mu m$. A prototype is fabricated using a cleanroom process. Then, a series of experiments are conducted to characterize the robot functional principle and its workspace. Preliminary results show a good agreement and confirm theoretical and FEA analysis expectations. The functional principle is demonstrated by generating elementary displacement while the workspace is validated by generating 169 stable positions with a step of 4.125 $\mu m$ and a resolution of 150 nm.

Future work will focus on the force characterization of the microrobot and the path planning. It would also concern the application of the robot for micromanipulation inside a confined environment.

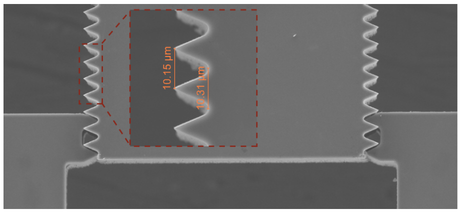

Fig. 15. Multistable teeth mechanism.

## VIII. ACKNOWLEDGMENT

This work has been supported by the EIPHI Graduate school (contract "ANR-17-EURE-0002") and the Labex ACTION project (contract ANR-11-LABX-01-01). It has been partly supported by the French RENATECH network and its FEMTO-ST technological facility. This work has been also partially supported by the Bourgogne Franche-Comté region project COMPACT.

## REFERENCES

[1] Régnier S, and Chaillet N, "Microrobotics for Micromanipulation", Wiley-ISTE, publisher, 2010.

[2] Rakotondrabe M, Haddab Y, Lutz P, "Quadrilateral modeling and robust control of a nonlinear piezoelectric cantilever", IEEE Trans Control Syst Technol 17 (T-CST) 17(3):528-539, 2009.

[3] M. Rakotondrabe, C. Clevy and P. Lutz, "Hysteresis and vibration compensation in a nonlinear unimorph piezocantilever", in IEEE/RSJ-IROS (International Conference on Intelligent Robots and Systems), Nice, France, pp. 558-563, 2008.

[4] G.S. Chirikjian, "A Binary Paradigm for Robotic Manipulators", in IEEE International Conference on Robotics and Automation, San Diego, CA, 1994, pp. 3063-3069

[5] Y. Wu, G. Ding, C. Zhang, J. Wang, S. Mao, and H. Wang, "Design and implementation of a bistable microcantilever actuator for magnetostatic latching relay," Microelectron. J., vol. 41, no. 6, pp. 325-330, Jun. 2010.

[6] Q. Chen, Y. Haddab, and P. Lutz, "Microfabricated bistable module for digital microrobotics," J. Micro-Nano Mechatron., vol. 6, no. 12, pp. 1-12, Feb. 2011.

[7] Q. Chen, Y. Haddab and P. Lutz "Characterization and control of a monolithically fabricated bistable module for microrobotic applications", in IEEE/RSJ- IROS (International Conference on Intelligent Robots and Systems), pp. 5756-5761, 2010

[8] H. Hussein, V. Chalvet, P. LeMoal, G. Bourbon, Y. Haddab and P. Lutz, "Design optimization of bistable modules electrothermally actuated for digital microrobotics", IEEE/ASME International Conference on In Advanced Intelligent Mechatronics (AIM), pp. 1273-1278, 2014.

[9] P. Wang and Q. Xu, ”Design and Testing of a Flexure-Based Constant-Force Stage for Biological Cell Micromanipulation,” in IEEE Transactions on Automation Science and Engineering, vol. 15, no. 3, pp. 1114-1126, July 2018, doi: 10.1109/TASE.2017.2733553.

[10] Y. Wei and Q. Xu, ”Design and Testing of a New Force-Sensing Cell Microinjector Based on Small-Stiffness Compliant Mechanism,” in IEEE/ASME Transactions on Mechatronics, doi: 10.1109/TMECH.2020.3003992..

[11] Q. Xu, ”Design of a large-stroke bistable mechanism for the application in constant-force micropositioning stage”, J. Mech. Robot., vol. 9, no. 1, p. 011006, 2017.

[12] M. Rakotondrabe, Y. Haddab and P. Lutz, ”Voltage/Frequency Proportional Control of Stick-Slip Micropositioning Systems,” in IEEE Transactions on Control Systems Technology, vol. 16, no. 6, pp. 1316-1322, Nov. 2008, doi: 10.1109/TCST.2008.917232.

[13] R. Buchi, W. Zesch, A. Codourey et R. Siegwart, ”Inertial drives for micro- and nanorobots: Analytical study”, SPIE’s, Intelligent Systems and Advanced Manufacturing, Philadelphia, USA, 23-26 octobre 1995.

[14] Chen IM, Gao SH. ”Locomotive gait generation for Inchworm like robots using finite state approach”, Robotica 19(5):535-542, 2001.

[15] G. Chen, Q. T. Aten, S. Zirbel, B. D. Jensen, and L. L. Howell, ”A Tristable Mechanism Configuration Employing Orthogonal Compliant Mechanisms”, J. Mech. Robot., vol. 2, no. 1, pp. 014501–6, Nov. 2009.

[16] D. S. Contreras and K. S. J. Pister, ”Dynamics of electrostatic inchworm motors for silicon microrobots”, 2017 International Conference on Manipulation, Automation and Robotics at Small Scales (MARSS), Montreal, QC, 2017, pp. 1-6.

[17] V. Chalvet, Y. Haddab, P. Lutz, ”A microfabricated planar digital microrobot forprecise positioning based on bistable modules”, IEEE Trans. Robot. 29 (June(3)) (2013) 641–649.

[18] H. Hussein, I. Bouhadda, A. Mohand-Ousaid, G. Bourbon, P. L. Moal, Y. Haddab, and P. Lutz, ”Design and fabrication of novel discrete actuators for microrobotic tasks”, Sensors and Actuators A: Physical, Volume 271, Pages 373-382, 2018.

[19] I. Bouhadda, A. Mohand-Ousaid, H. Hussein, G. Bourbon, P. L. Moal, Y. Haddab and P. Lutz, ”Repeatability and reproducibility analysis of a multistable module devoted to digital microrobotics”, IEEE RSJ International Conference on Intelligent Robots and Systems (IROS 2018) / Madrid, Spain (2018, Pages 4889-4894).

[20] Howell, L.L., ”Compliant Mechanisms”, John Wiley & Sons, Inc., New York, 2001.

[21] N. Lobontiu, J.S.N. Paine, E. Garcia, M. Goldfarb, ”Corner filleted flexure hinges”, ASME Journal of Mechanical Design, 123, pp. 346-352, 2001.

[22] JCGM (Organization), ”International vocabulary of metrology: basic and general concepts and associated terms (VIM),” 2012.